A Complete Equivalent Circuit for Linear Induction Motors with Laterally Asymmetric Secondary for Urban Railway Transit

Gang Lv, *IEEE Member*, Dihui Zeng, *IEEE Member*, Tong Zhou, Michele Degano, *IEEE Member*

***Abstract*—Since the linear induction motor commonly work with a laterally asymmetric secondary as it is applied to pull rail vehicles, this paper presents a complete equivalent circuit model considering the asymmetry to predict thrust, vertical and transversal forces. First, six correction factors are presented to quantify the variations in the air-gap magnetic flux and secondary induced current as the linear induction motor operating with a laterally asymmetric secondary. Second, it develops a circuit model based on the existing T-model for the rotary induction motor and two correction factors for the magnetizing branch, which is used to indicate the electromagnetic variations in the air-gap flux and secondary plate due to the asymmetry. Third, the mathematical expressions for the thrust, vertical and transversal forces are derived by applying the equivalent circuit model. Then, the six correction factors are calculated with a prototype motor, and the results of them are comprehensively analyzed. Finally, the characteristics in the prototype motor are calculated with the mathematical expressions in a range of rated speed，and validated by the experimental measurements carried out on a test rig and line for linear motors.**

***Index Terms*—Linear induction motors, equivalent circuit, end effects, asymmetric secondary, thrust, vertical force, transversal force**

NOMENCLATURE

τ_p	Pole pitch
g_e	Electromagnetic gap
ω_1	Supply angular frequency
ω_2	Slip angular frequency
I_1	Primary winding current
I_m	Magnetizing current
I_{21}	Secondary current
V_s	Power voltage
j_{2x}	x-component of secondary eddy current in aluminum plate
j_{2y}	y-component of secondary eddy current in aluminum plate
Bz	z-component of air-gap magnetic flux density
κ_1	Distribution factor to air-gap magnetic flux
κ_2	Ratio of air-gap magnetic flux in narrow side to total air-gap magnetic flux
κ_3	Ratio of air-gap magnetic flux in wide side to total air-gap magnetic flux
κ_4	Distribution factor to y-component of I_{21}
κ_5	Ratio of x-component to y-component of secondary eddy current in narrow side
κ_6	Ratio of x-component to y-component of secondary eddy current in wide side
h_2	Secondary width
L	Total primary length
c_1	Overhang of primary winding
c_2	Overhang of secondary plate
Δy	Secondary displacement
v_1	Synchronous velocity
v_2	Primary running velocity
T_v	Real time for moving over the primary length
T_b	Secondary time constant
m_1	Number of phases
f_1	Power frequency
s	Slip
F_x	Thrust
F_y	Transversal force
F_z	Vertical force
F_{z1}	Attractive vertical force
F_{z2}	Repulsive vertical force

I. INTRODUCTION

LINEAR induction motors (LIMs) are widely applied in urban transportation system, e.g. linear metro, low- and medium speed maglev train, due to their own advantages: propelling vehicle without any transmission gear, low vibration noise, etc. [1]. In the application of the transportation system, owing to the limitation of the motor manufacture and rail construction, LIMs usually work with a non-ideal operating condition, e.g. variable air-gap length, discontinuous secondary [2], asymmetric secondary [3-4], etc. Different from rotary induction motors (RIMs), the longitudinal and transversal end effects are the crucial phenomena in LIMs, and electromagnetic field analysis for LIMs becomes significantly important [5].

In recent decades, many researchers mainly focused on motor control methods [6-8], equivalent circuits and parameter estimation [10-11], and electromagnetic field analysis and motor design [12-15]. For the analysis of electromagnetic field, the quasi-1D [16] or 2D methods are currently the mainstream approaches to handle the longitudinal end effect, the correction

This work was supported in part by the National Natural Science Foundation of China through Project 51377009 and 51777009.

G. Lv and T. Zhou are with the Sch. of E.E., Beijing Jiaotong Univ., Beijing 100044, China (e-mail: ganglv@bjtu.edu.cn, zhoutong@bjtu.edu.cn)

D. Zeng is with the Key Laboratory of Power Electronics and Electric Drive, Institute of E. E., Chinese Academy of Sciences, Beijing 100190, China (e-mail: zengdh@mail.iee.ac.cn)

M. Degano is with the Dept. of E.E.E., Univ. of Nottingham, UK NG7 2RD and Ningbo 315000, China (e-mail: michele.degano@nottingham.ac.uk)

factors of which are presented to take skin effect, magnetic saturation, transversal end effect into consideration. In [3], the authors proposed a 3D analytical method based on space harmonic techniques, which takes longitudinal and transversal end effects into account.

In Fig.1(a), when the train is running on the straight rails, the LIM installed under the carriage works with a laterally symmetric secondary, the transversal forces on both sides, which is divided by the center line, cancel each other out, then, the resultant transversal force is equal to zero. Since a laterally asymmetric secondary is applied as the train is running on the curve rails, as shown Fig.1(b), the magnitude of transversal forces on both sides is not equal, then the resultant transversal force will be more than zero. The resultant transversal force that is not equal to zero has negative impacts on the train operation, e.g. intensifying rail abrasion, destabilizing steering system, etc. Furthermore, the characteristics in the LIM working with an asymmetric secondary are also be affected by the asymmetry. Therefore, a decoupling control strategy for eliminating the transversal force and compensate the loss of characteristics due to the asymmetry is practically important to linear metro or maglev train. Generally, the mathematical model for LIMs in the control theory is based on the equivalent circuit, hence, deriving an equivalent circuit model is critical to achieve the decoupling control strategy.

In [17-20], the equivalent circuit models are basically inherited from the classic T-type circuit for RIMs, however, the transversal force cannot be predicted by this circuit as the train driven by LIMs is working on the curve rails. In [21], for simplifying complicate calculation, it proposes an intelligible circuit model for LIMs, which is so-called Duncan model in this paper, by inheriting T-type circuit. In the model, it assumes the longitudinal air-gap magnetic flux distribution is described by an exponential function, and the further improvements based on Duncan model are presented in [22-23]. Nevertheless, owing to the symmetric secondary assumed in Duncan model, the transversal force and the other motor characteristics affected by the asymmetry cannot be obtained. Therefore, deriving an equivalent circuit to solve the issue that the existing circuit models cannot predict the transversal force and the influences of the asymmetric secondary on the characteristics in LIMs is significantly important to the LIM control for the full operation conditions.

In [24], the authors presented an improved equivalent circuit to consider the characteristics affected by the laterally asymmetric secondary, and managed to describe those effects in the equivalent circuit by using some exponential correction factors. Indeed, the exponential function method can roughly estimate the changes of components in the circuit model when the asymmetric secondary is applied in. However, this method is inaccurate and without any practical significances.

In this paper, on the basis of the electromagnetic field analysis of LIMs, it presents some correction factors to describe the variations due to the asymmetric secondary and correct the components in the equivalent circuit. Besides, the correction factors are all relevant to the parameters of LIMs, and its prediction accuracy may be significantly improved. Based on [23], this paper firstly comprehensively analyses the variations in the air-gap magnetic flux and secondary induced current due to the asymmetric secondary, and proposes six correction factors ($\kappa_{1\text{-}6}$), which is based on the electromagnetic field quantity expressions and derived from 3D analytical method, to describe the variations in circuit model instead of the electromagnetic field analytical method. Second, it proposes a complete equivalent circuit considering the LIM operating with a laterally asymmetric secondary and the correction factors to the magnetizing branch reflecting the variation in the air-gap magnetic flux and the electromagnetic power losses. Third, the mathematical expressions for the thrust, vertical and transversal forces are given by using the complete equivalent circuit. Then, a prototype LIM is applied to calculate the six correction factors ($\kappa_{1\text{-}6}$) and the motor characteristics with the complete circuit model. Finally, the calculated results are verified by the experimental measurements.

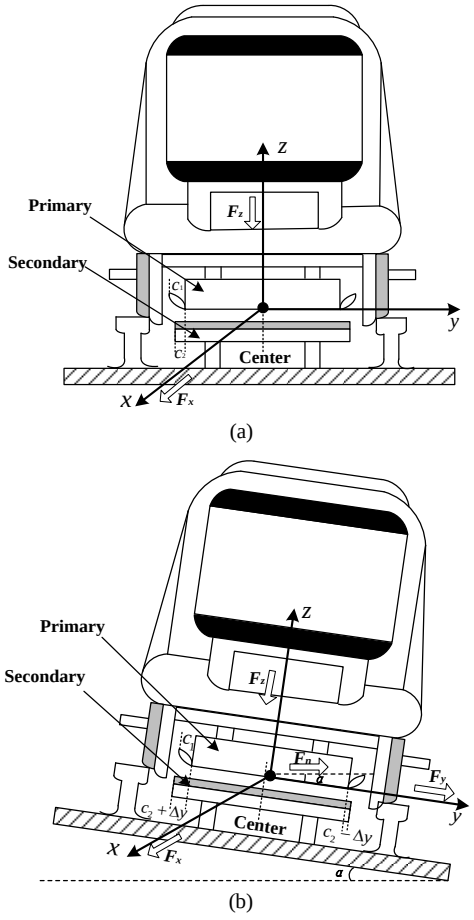

Fig. 1. Train driven by LIMs: (a) Train on straight rails (b) Train on curve rails

II. Analysis of Electromagnetic Field

In general, the classic equivalent circuit for induction motors, as shown in Fig.2, is derived from 1D field theory, which means the primary current I_1 and secondary current I_{21} only have the y-component(j_{2y}), whereas the x-component(j_{2x}) is not taken into consideration. In squirrel-cage IMs, the secondary (rotor) eddy current flows around the conductor, its path is an ideal rectangle, as shown in Fig.3(a). In Fig.3(a), only j_{2y} is existed in the active zone, therefore, j_{2x} may be ignored in the

analysis without any obvious calculation error. In LIMs, the secondary conductor is a piece of flattened aluminum or copper plate, and secondary induced current flows around the circle as a kind of ellipses, as shown in Fig.3(b). When the LIM works with an asymmetric secondary, the path of secondary induced current will be distorted with the asymmetry [24-25], as shown in Fig.3(c). In these two cases, the *x*-component of I_{21} cannot be negligible. Consequently, the assumptions based on the 1D field theory cannot consider the influences of the laterally asymmetric secondary on the electromagnetic characteristics in LIMs. Then, a method that makes secondary current relate to its *x*-component is presented as follows.

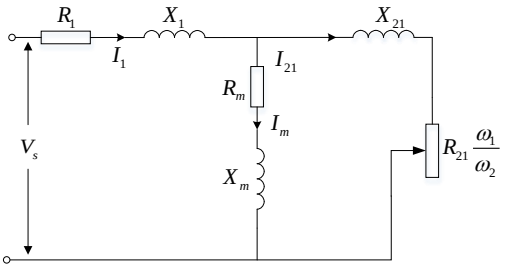

Fig. 2. T-type equivalent circuit for IMs

A. *Variation of Air-gap Magnetic Flux Density*

In [3], the mathematical expressions of the air-gap magnetic flux density are given, and it indicates the magnetic flux density along the *y*-direction tends to be U-shaped. In Fig.4, as the symmetric secondary is applied, the U-shaped curve is centerline symmetry, which is induced by the symmetric current path, as shown in Fig.3(b); as the asymmetric secondary is applied, the U-shaped curve becomes asymmetry. The maxima of the magnetic flux density in the narrow side (left side) increases while that in the wide side (right side) decreases. The asymmetric change of the magnetic flux density along the *y*-direction are primarily caused by the distortion of current path (c.f. Fig.3(c)). When the LIM works with an asymmetric secondary, a distortion factor κ_1 to the air-gap magnetic flux is defined by

$$\kappa_1 = \frac{\int_{-h_2/2-\Delta y}^{h_2/2-\Delta y}\int_{-L/2}^{L/2}\left|B_z(\Delta y)\right|dxdy}{\int_{-h_2/2}^{h_2/2}\int_{-L/2}^{L/2}\left|B_z(0)\right|dxdy} \tag{1}$$

where L is the primary core length; h_2 is the secondary width; $B_z(0)$ (T/m^2) is the *z*-component of the air-gap magnetic flux density produced with the symmetric secondary; $B_z(\Delta y)$ (T/m^2) is the *z*-component of the air-gap magnetic flux density when the asymmetric secondary is applied; Δy is the distance of the secondary lateral displacement.

The ratio κ_2 or κ_3 of the air-gap magnetic flux density in the narrow or the wide side to the total air-gap magnetic flux density are defined by

$$\kappa_2 = \frac{\int_{-\Delta y}^{h_2/2-\Delta y}\int_{-L/2}^{L/2}\left|B_z(\Delta y)\right|dxdy}{\int_{-h_2/2}^{h_2/2}\int_{-L/2}^{L/2}\left|B_z(\Delta y)\right|dxdy} \quad \kappa_3 = \frac{\int_{-h_2/2-\Delta y}^{-\Delta y}\int_{-L/2}^{L/2}\left|B_z(\Delta y)\right|dxdy}{\int_{-h_2/2}^{h_2/2}\int_{-L/2}^{L/2}\left|B_z(\Delta y)\right|dxdy} \tag{2}$$

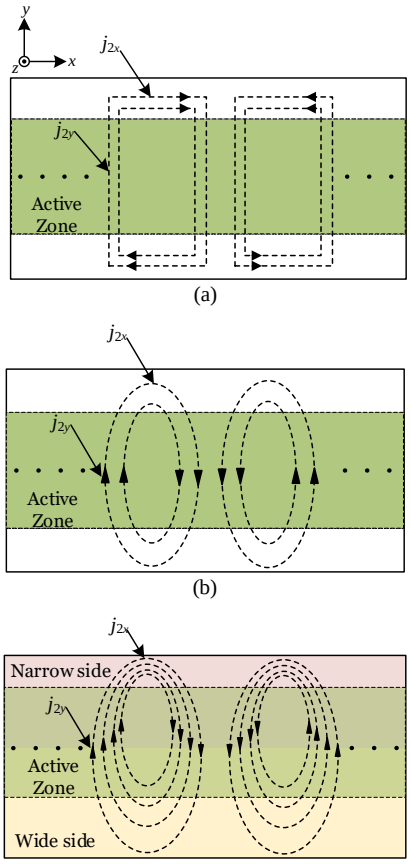

Fig. 3. Distribution of secondary induced current: (a) in squirrel-cage IMs (b) in LIMs with a symmetric secondary (c) in LIMs with an asymmetric secondary

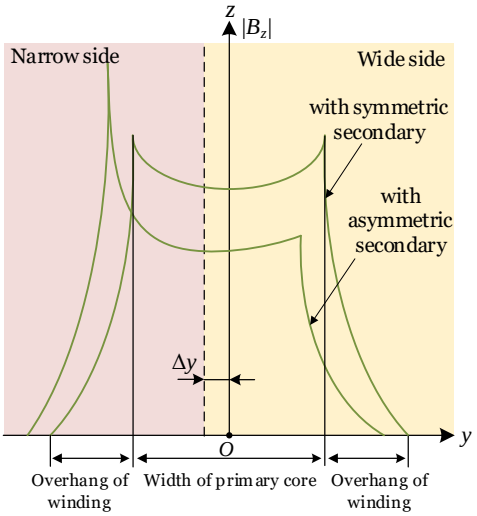

Fig. 4. Transversal air-gap magnetic flux density along the *y*-direction with the symmetric/asymmetric secondary

B. *Variation of Secondary Induced Current*

In [3], the mathematical expressions of the eddy current density are given, and it indicates the distribution of secondary eddy current varies with the secondary displacement. Besides, this variation will also be affected by the slip-frequency. In accordance with the unique phenomenon above, I_{21} needs to be varied with the secondary displacement. Since I_{21} is not relative to the *x*-component of I_{21}, this paper introduces a factor κ_4 to

correct I_{21} when it calculates the thrust in the LIMs with an asymmetric secondary, and the factor κ_4, which may also be called the distortion factor to the *y*-component of I_{21}, is defined by

$$\kappa_4 = \frac{\int_{-h_2/2-\Delta y}^{h_2/2-\Delta y}\int_{-L/2}^{L/2} \left|j_{2y}(\Delta y)\right|^2 dxdy}{\int_{-h_2/2}^{h_2/2}\int_{-L/2}^{L/2} \left|j_{2y}(0)\right|^2 dxdy} \tag{3}$$

where j_{2y} is the *y*-component of secondary induced current density in the aluminum plate.

Compared with secondary eddy current in Fig.3(b), in Fig.3(c), the *x*-component of the eddy current in the narrow side is dramatically increased, while that in the wide side is significantly decreased. Therefore, in this paper, it also introduces two factors κ_5 (and κ_6) to describe the *x*-component ratio to the *y*-component of the eddy current density in the narrow side (and the wide side), and they are defined by

$$\kappa_5 = \frac{\int_{-\Delta y}^{h_2/2-\Delta y}\int_{-L/2}^{L/2} \left|j_{2x}(\Delta y)\right| dxdy}{\frac{1}{2}\int_{-h_2/2-\Delta y}^{h_2/2-\Delta y}\int_{-L/2}^{L/2} \left|j_{2y}(0)\right| dxdy} \qquad \kappa_6 = \frac{\int_{-h_2/2-\Delta y}^{-\Delta y}\int_{-L/2}^{L/2} \left|j_{2x}(\Delta y)\right| dxdy}{\frac{1}{2}\int_{-h_2/2-\Delta y}^{h_2/2-\Delta y}\int_{-L/2}^{L/2} \left|j_{2y}(0)\right| dxdy} \tag{4}$$

where j_{2x} is the *x*-component of secondary induced current density in the aluminum plate.

III. Equivalent Circuit Model and Forces

A. Equivalent Circuit

All of the existing equivalent circuit for LIMs [19-25] cannot be utilized to obtain the transversal force and consider the variations in the electromagnetic field when the asymmetric secondary is applied. Therefore, for obtaining the complete characteristics in LIMs, the equivalent circuit should take the longitudinal and transversal end effects, and the influences of the asymmetric secondary on secondary induced current path and the variable air-gap magnetic flux into consideration.

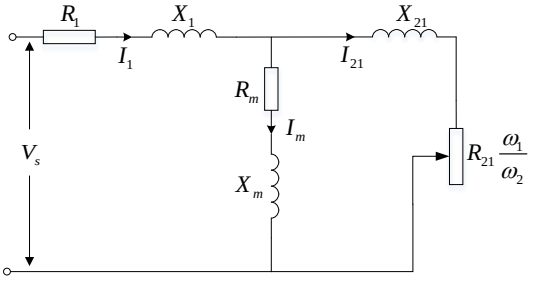

Fig. 5. The complete equivalent circuit for LIMs

The complete equivalent circuit considering the thrust, vertical and transversal forces is shown in Fig.5. Since the secondary demagnetizing current impedes the buildup of the total air-gap magnetic flux, the magnetizing inductive reactance X_m is corrected by a factor K_{Lmd} that represents the magnitude of the air-gap magnetic flux decay due to the end effect. Owing to the distortion of the air-gap magnetic flux when the secondary is displaced, $K_{Lmd}X_m$ is divided into two parts, as shown in the dash frame in Fig.5, and these two presents the left and right side defined by the central line (c.f. Fig.1) on the transversal cross-section (*yz*-plane), respectively. Likewise, an extra resistance R_{21}, which implies the loss of the secondary demagnetizing current, is linked the slip and the secondary displacement by a correction factor K_{R21d}, and it is connected in the series with the magnetizing branch. Plus, the secondary resistance is corrected to consider the asymmetry as well.

In [21], the secondary time constant T_b and the time taken for the motor traverse a point on the rail T_v are given. Then, a normalized time scale Q is obtained by

$$Q = T_v / T_b = \frac{LR_{21}}{(L_m + L_{21})v_2} \tag{5}$$

where L is the length of the primary core; v_2 is running velocity of the primary; L_m and L_{21} are the magnetizing inductance and the secondary leakage inductance, respectively.

In (5), Q is dimensionless, and it represents the motor length on the normalized time scale. In [23], the mathematical models of the normalized air-gap magnetic flux and secondary induced current are given, however, those models cannot be directly applied for the analysis of the LIM working with an asymmetric secondary. Since the secondary displacement changes the amplitude of the air-gap magnetic flux and secondary eddy current, their distribution model may be multiplied or divided by a factor κ_1. Then, the normalized air-gap magnetic flux model considering the asymmetry may be modified by

$$f_a'(t_1) = \kappa_1 \frac{1 - e^{-t_1}\cos\delta t_1}{1 + e^{-\frac{\pi}{\delta}}} \tag{6}$$

where t_1 is the normalized time; $\delta = a \cdot s$, s is the slip, and a is a coefficient which is discussed in [23].

And, the normalized secondary induced current model considering the asymmetry may be modified by

$$f_s'(t_1) = \frac{1}{\kappa_1}\left(\frac{-1 + e^{-t_1}\cos\delta t_1}{1 + e^{-\frac{\pi}{\delta}}} + 1\right) \tag{7}$$

Owing to the variation in the mathematical models above, the correction factors K_{Lmd} and K_{R21d} in the magnetizing branch may be derived by the derivation methods of K_{Lm} and K_{R21} presented in [23], and they are given by

$$K_{Lmd} = \frac{e^{-Q}\left[\begin{array}{l} e^{\frac{\pi}{\delta}}\left(\kappa_1\delta^2 Q + \kappa_2 Q - 1\right) - \delta\sin\delta Q - \\ e^{Q}\left(1+\delta^2\right)\left(Q - \kappa_1 Q\right) + \cos\delta Q \end{array}\right]}{\kappa_1 Q\left(1+\delta^2\right)\left(1 + e^{\frac{\pi}{\delta}}\right)} \tag{8}$$

$$K_{R21d} = \frac{e^{-2Q}}{4\left(1+\delta^2\right)\left(1+e^{\frac{\pi}{\delta}}\right)^2 \kappa_1^2 Q} \times \left\{\begin{array}{l} 4Q\left(1+\delta^2\right)e^{2Q} + 8e^{\frac{\pi}{\delta}+Q}\left(e^{Q} - \cos\delta Q + \delta\sin\delta Q\right) + e^{\frac{2\pi}{\delta}}\left[-1\right. \\ \left. -\delta^2 + e^{2Q}\left[\begin{array}{l} 2 + \delta^2 + 2\kappa_1^4\left(1+\delta^2\right) - 4e^{Q}\kappa_1^4\left(1+\delta^2\right)\cos\delta Q \\ +2\kappa_1^4\left(1+\delta^2\right)\cos^2\delta Q - \cos 2\delta Q + \delta\sin 2\delta Q \end{array}\right]\right] \end{array}\right\} \tag{9}$$

B. Thrust

Thrust F_x consists of two components: the positive thrust F_{x1} and the negative thrust F_{x2}. The F_{x1} is produced by the slip current, and its direction is consistent with the direction of motor motion. Since F_{x1} directly produces mechanical power, according to the principle of energy conversion, it is given by

$$F_{x1}=3I_{21}^2R_{21}\kappa_4\frac{\pi}{\omega_2\tau_p} \tag{10}$$

In (10), κ_4 is applied to indicate the influence of the secondary displacement on the thrust. The F_{x2} is produced by the demagnetizing loss, it is always in the opposite direction of F_x. The work done by F_{x2} can be expressed by ohmic loss due to R_{21d} connected in series to the magnetizing branch. Then, it is given by

$$F_{x2}=\frac{3I_m^2K_{R21d}R_{21}}{v_2} \tag{11}$$

In (11), K_{R21d} is dependent upon κ_4, and it is also affected by the secondary displacement. According to (10)(11), F_x in the LIM may be obtained by

$$F_x=F_{x1}-F_{x2} \tag{12}$$

C. Vertical Force

In RIMs or double-sided LIMs (DLIMs), despite of existence of the vertical force, the force is negligible due to their axisymmetric or symmetric structure. However, in single-sided LIMs (SLIMs), the force must be considered as an important part of characteristics in SLIMs. In general, the vertical force F_z consists of two components: attractive force F_{z1} and repulsive force F_{z2}, and the attractive one dominates the F_z. On the basis of principle of the electromagnetism, the F_{z1} is emerged by the interaction between the air-gap magnetic flux and the secondary back-iron.

In [23], the r.m.s value of the instantaneous magnetizing current (I_{mer}) is given, however, the air-gap magnetic flux will be distorted with the variation of the secondary displacement. Then, I_{mer} may be corrected by κ_1, and it is redefined by

$$I_{mer}^{'}=\sqrt{\frac{I_m^2}{Q}\int_0^Q\left[f_a^{'}(t_1)\right]^2dt_1} \tag{13}$$

Owing to the magnetic energy stored in the air-gap, the attractive force F_{z1} is given by

$$F_{z1}=K_{az}L_mI_{mer}^{'2}=K_{az}\kappa_1^2L_m\left[I_mf_z(Q)\right]^2 \tag{14}$$

where the K_{az} can be determined from dynamic tests on the prototype motor.

The repulsive force F_{z2} is formed by the interaction between the *y*-component of primary current and the *y*-component of secondary eddy current, which is decayed by the asymmetry, as shown in Fig.3(c). Then, F_{z2} may be corrected by κ_4, and it is obtained by

$$F_{z2}=K_{rz}\kappa_4\frac{I_{21}^2}{g_e} \tag{15}$$

where the K_{rz} can be determined from dynamic tests on the prototype motor.

According to (14)(15), F_z in the LIM is given by

$$F_z=F_{z1}-F_{z2} \tag{16}$$

D. Transversal Force

In RIMs, the position of the rotor related to the stator is mechanically fixed. However, in DLIMs and SLIMs, the secondary is laterally movable, and it has no mechanical constraint to the primary core. When the LIM works with a laterally symmetric secondary, the transversal forces in the two sides are equal, and the resultant transversal force equals zero. When a laterally asymmetric secondary is applied in the LIM, the transversal forces respectively produced by left and right side are not equal, and they are in the opposite directions. Therefore, the resultant transversal force is gradually emerged, and it increases with the secondary displacement. Moreover, the transversal force results in negative effects for vehicles, e.g. intensify the abrasion of the wheels and rails. Generally, the transversal force F_y may be divided into two components: transversal attractive force F_{y1}, transversal repulsive force F_{y2}.

Based on the tensor theory, the F_{y1} is formed by the interaction between the back-iron and the *y*-component of the air-gap magnetic flux produced by the magnetizing current I_m. Thus, the transversal attractive force $F_{y11/y12}$ for each side may be respectively corrected by κ_2 and κ_3, and they are given by

$$\begin{cases} F_{y11}=K_{ay}\kappa_2L_mI_{mer}^{'2}=K_{ay}\kappa_2\kappa_1^2L_m\left[I_mf_z(Q)\right]^2 \\ F_{y12}=K_{ay}\kappa_3L_mI_{mer}^{'2}=K_{ay}\kappa_3\kappa_1^2L_m\left[I_mf_z(Q)\right]^2 \end{cases} \tag{17}$$

where the K_{ay} can be determined from dynamic tests on the prototype motor.

The F_{y2} is produced by the interaction between the *x*-component of I_1 and the *x*-component of I_{21}. In Fig.3(c), the *x*-component of I_{21} increases in the narrow side while decays in the wide side. Then, the transversal repulsive force $F_{y21/y22}$ for each side may be respectively corrected by κ_5 and κ_6, and they are obtained by

$$\begin{cases} F_{y21}=K_{ry}\kappa_5\dfrac{I_{21}^2}{g_e} \\ F_{y22}=K_{ry}\kappa_6\dfrac{I_{21}^2}{g_e} \end{cases} \tag{18}$$

where K_{ry} can be determined from dynamic tests on the prototype motor.

According to (17)(18), the F_y in LIMs is given by

$$F_y=\left[F_{y11}-F_{y12}\right]-\left[F_{y21}-F_{y22}\right] \tag{19}$$

IV. Experiments and Validation

In the experimental measurement, the data acquisition system and the test apparatus for the SLIM, i.e. rig and line, as shown in Fig.6, are experimentally manufactured to validate the results calculated by the complete equivalent circuit. In Fig.6(a), the prototype SLIM (c.f. Table I) is fed by a converter installed under the carriage. The converter is able to change its output voltage (AC0~1100V) and power frequency (0~35Hz), and its input voltage is DC1500V sourced from contact rail. When the experimental measurement is implementing, the data acquisition system programmed with LabView® is working to

obtain the raw data, i.e. voltage, current, thrust, vertical force, transversal force (lateral force), velocity and etc., with several sensors, the specification of which is listed in Table II. For simulating the prototype SLIM with an asymmetric secondary run on the straight test line, the prototype SLIM was laterally asymmetrically installed under the test bogie with several displacements of the secondary, and the displacement normally is no more than 3 cm.

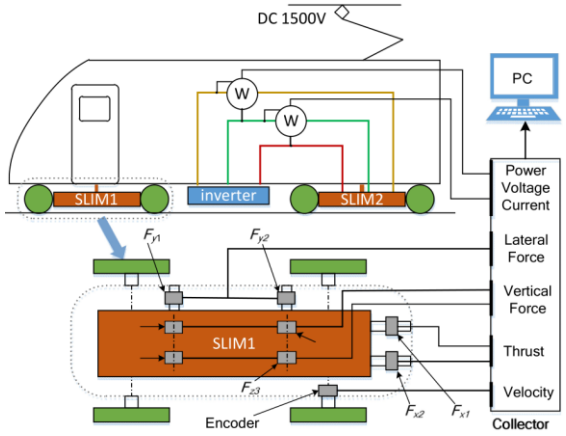

(a)

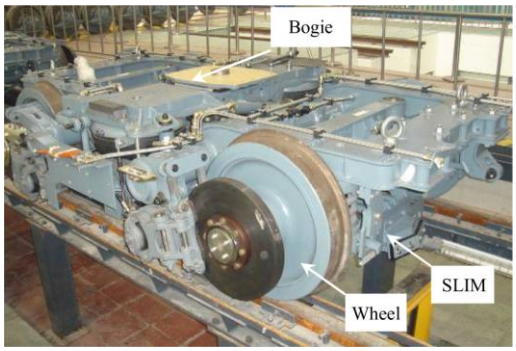

(b)

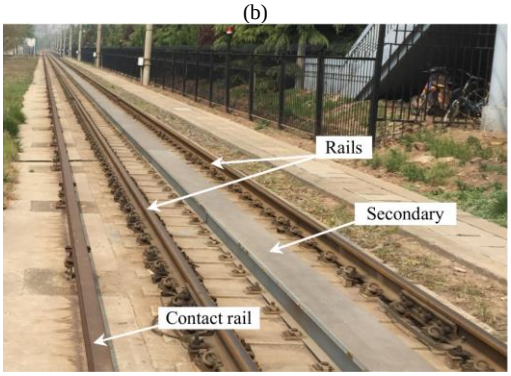

(c)

Fig. 6. Experimental measurements: (a) acquisition system (b) test rig (c) test line

In Figs.7-10, the correction factors κ_1 to κ_6 versus the slip with different secondary displacements at I_1=160 A, f_1=35 Hz are given, these factors are calculated with the parameters of the prototype SLIM. In Fig.7, it shows the larger value of the secondary displacement results in a big distortion of the air-gap magnetic flux, the maxima and minima of κ_1 reach 1.01 and 0.984, respectively. When $s\leq0.4$, the integral area of the distorted air-gap magnetic flux caused by the asymmetric secondary is smaller than that of the symmetric air-gap magnetic flux. When $s>0.4$, it is a completely opposite case.

TABLE I
SPECIFICATIONS OF PROTOTYPE SLIM

Symbol	Quantity	Value	Unit
m	Number of phases	3	
p	Number of poles	8	
τ_p	Pole pitch	292	mm
c_1	Overhang of primary winding	130	mm
β	Coil pitch	7/9	
L	Total primary length	2500	mm
d_1	Back iron plate thickness	25	mm
d_2	Aluminum plate thickness	7	mm
h_1	Primary width	320	mm
h_2	Secondary width	480	mm
h_3	Secondary overhang	60	mm
h_4	Back iron width	360	mm
d_3	Thickness of secondary overhang	32	mm
g_1	Gap length	10	mm
V_1	Rated input voltage	1100	V
I_1	Rated R.M.S current	160	A
f_1	Rated power frequency	35	Hz
R_1	Resistance of the primary windings	198	mΩ
L_1	Leakage Inductance of primary windings	4.34	mH
R_{21}	Secondary resistance referred to primary	362	mΩ
L_{21}	Secondary leakage inductance referred to primary	0.22	mH
L_m	Magnetizing inductance	32.2	mH

TABLE II
SPECIFICATION OF SENSORS

Item	Ranges	Output	Non-linearity
Voltage	-2 kV~2 kV	-5 V~5 V	0.5% F.S.
Current	-2 kA~2 kA	-4 V~4 V	1% F.S.
Thrust	-20 kN~20 kN	-5 V~5 V	3% F.S.
Vertical force	-100 kN~100 kN	-5 V~5 V	5% F.S.
Transversal force	-5 kN~5 kN	-5 V~5 V	3% F.S.

In Fig.8(a), κ_2 increases with the slip s, and its growth rate is proportional to the secondary displacement, it reaches the peak of 0.67 at s=1 and Δy=3 cm, which means the average of the air-gap magnetic flux in the narrow side is larger than that of the normal air-gap magnetic flux. In Fig.8(b), since κ_3 indicates the air-gap magnetic flux in the wide side, the curves are just opposite to those in narrow side, and its minima is 0.33 at s=1 and Δy=3 cm.

In Fig.9, it reveals the secondary displacement will reduce the y-component of secondary induced current, and the decay of the curve is intensified by the displacement. As $s\leq0.4$, κ_4 is more sensitive to s, and it reaches the bottom of 0.977 at s=0 and Δy=3 cm. Plus, κ_4 directly indicates the secondary displacement reduces the thrust in LIMs.

In Fig.10(a), κ_5 decreases with the s, and its descending rate is inversely proportional to the secondary displacement, which means the larger displacement will result in a bigger portion of the x-component of secondary induced current in the narrow side, the curve of Δy=3 cm reaches its peak of 0.65 at s=0 and hits its lowest of 0.56 at s=1. In Fig.10(b), since κ_6 indicates the ratio of the x-component in the wide side, the descending rate of

curves are opposite to those in narrow side, and its maxima and minima are 0.59 and 0.5 at Δy=3 cm, respectively.

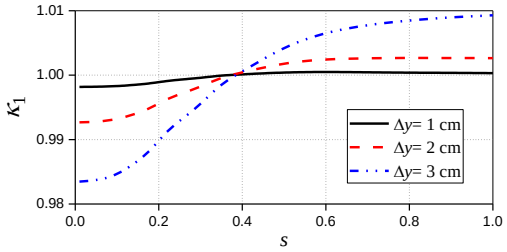

Fig. 7. κ_1 *v.s.* slip with different Δy

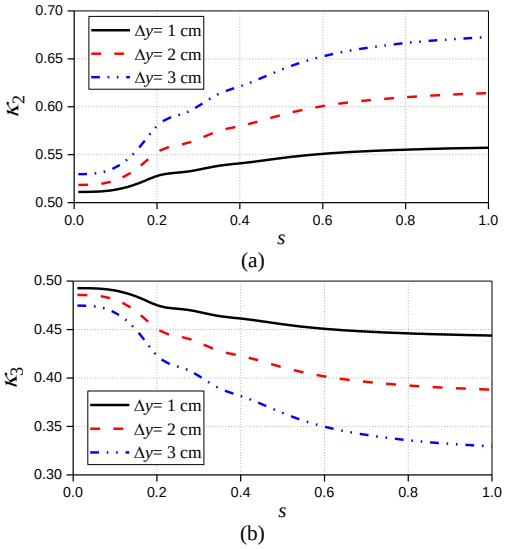

Fig. 8. κ_2 and κ_3 *v.s.* slip with different Δy: (a) Narrow side (b) Wide side

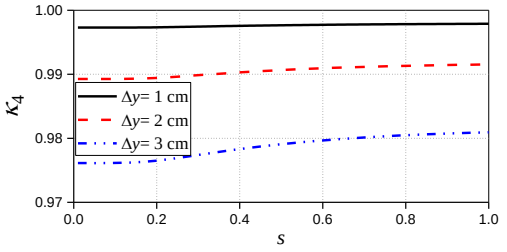

Fig. 9. κ4 v.s. slip with different Δy

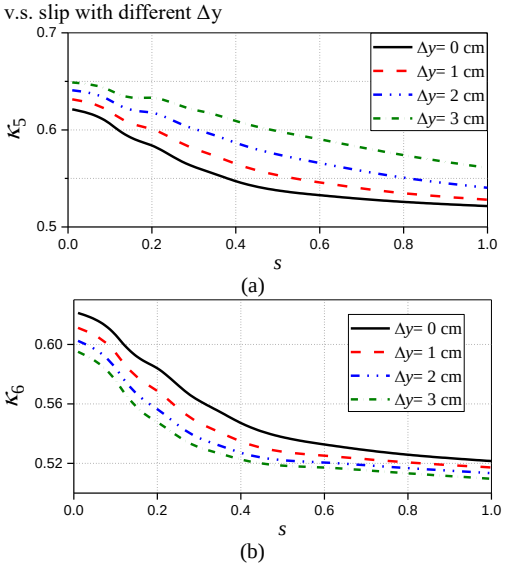

Fig. 10. κ_5 and κ_6 *v.s.* slip with different Δy: (a) Narrow side (b) Wide side

In Fig.11, the results for F_x, F_z and F_y calculated by the complete equivalent circuit model for LIMs are validated with experimental measurements. To evaluate the performance of the complete equivalent circuit, the prototype SLIM is fed by a variable voltage and variable frequency (VVVF) drive, and the characteristics are obtained when the input current I_1 equals rate current (160 A) and input frequency f_1 equals 5, 15, 25 and 35 Hz. In this case, the three forces are a function of the velocity or slip-frequency. Besides, the transversal force and its effects on the thrust and vertical force is obtained by applying different degrees of the secondary displacement.

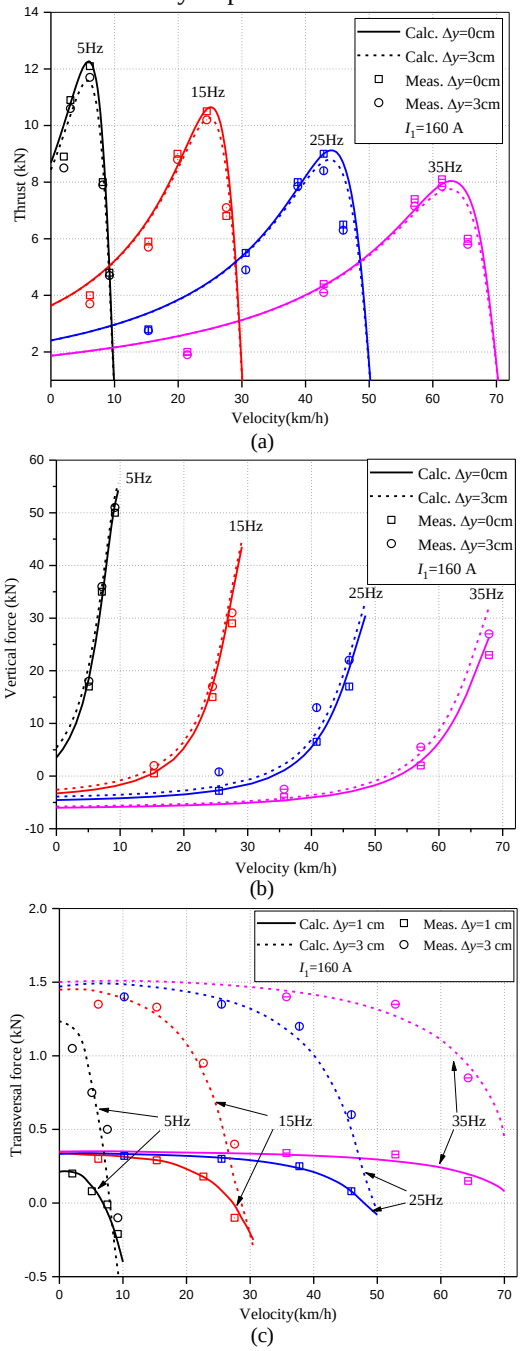

Fig. 11. Force characteristics: (a) Thrust (b) Vertical force (c) Transversal force

In Fig. 11(a), owing to the limited power in the LIM and the longitudinal end effect, the average of each curve decreases step by step with the increasing of the supply frequency. As an induction motor, the thrust will sharply decline while the slip is approaching zero. Therefore, the motor drives should

dynamically adjust the frequency with the operating velocity so that it produces a constant thrust continuously. Since the asymmetry causes the distortion of secondary induced current and air-gap magnetic flux, the thrust is slightly decreased, and the calculated results basically accords with measurements.

In Fig. 11(b), the positive value is attractive force, and the negative value is repulsive force. In this prototype motor, the vertical force is usually attractive one in the slip region of the typical operating condition ($s < 0.5$). Owing to the distortion of secondary induced current (the x-component is reduced) in the asymmetric secondary, the repulsive component of the vertical force decreases. Then, the resultant vertical force is increased by the asymmetry.

In Fig.11 (c), the positive value is transversal repulsive force (decentralizing force), and the negative value is transversal attractive force (centralizing force). Owing to the distortion of the air-gap magnetic flux and secondary induced current in the asymmetric secondary, the repulsive and attractive component of the transversal force is varied with the asymmetry. In this prototype motor, therefore, the transversal forces dramatically increase with the secondary displacement. Besides, each curve of the transversal forces decreases with the running speed, which is similar to trend of the thrust. In Table III, the calculation errors are presented, and the maximum errors are around 25%, the average errors are less than 10%. In Fig.11, the larger calculation error usually exists in the region $s<0.5$, since the nonlinear phenomenon is more obvious in this region. Besides, owing to the disturbance of the vibration and force surge during the experimental measurement, the random measurement error is inevitable, which is cause of the maximum error.

TABLE III
CALCULATION ERRORS

Item	Maximum error	Average error
Thrust (F_x)	27.12 %	9.93 %
Transversal force (F_y)	26.75 %	7.87 %
Vertical force (F_z)	24.91 %	8.56 %

The efficiency and secondary power factor at rated operating velocity points are shown in Fig.12. The trend of efficiency and secondary power factor is very consistent, and their value is lower in the low speed region and gradually increases as the speed increases. Since the asymmetry increases secondary induced current loss, the motor efficiency is reduced by approximately 5%. Similarly, the secondary power factor in the symmetric secondary is also larger than that in the asymmetry, and this difference becomes more obvious as the speed increases. In addition, the calculation error will increase as Δy increases, since the nonlinearity of secondary induced current and the electromagnetic field distribution in the LIMs becomes higher.

V. CONCLUSIONS

In this paper, a complete equivalent circuit model considering the laterally asymmetric secondary provides a practical method for predicting force characteristics in LIMs, e.g. thrust, vertical and transversal forces. It fixes the issue that the existing equivalent circuit cannot analyze the transversal force and influence of the asymmetric secondary on electromagnetic characteristics in LIMs. The calculated results were verified by the experimental measurements, and the average calculation errors are less than 10%. In future works, the calculation accuracy could be improved by considering more nonlinear phenomena in the analytical procedures.

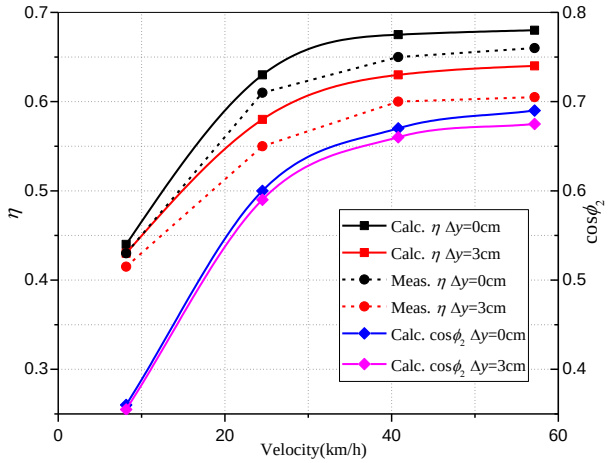

Fig.12 Efficiency and secondary power factor

REFERENCES

[1] I. Boldea, "Linear Electric Machine, Drives, and MAGLEVs Handbook". *CRC Press, U.K: London*, 2013, pp. 55–128.

[2] G. Lv, S. Yan, D. Zeng, and T. Zhou. "An Equivalent Circuit of the Single-sided Linear Induction Motor Considering the Discontinuous Secondary," *IET Elect. Power App.*, vol. 13, no. 1, pp. 31-37, 2018

[3] G. Lv, D. Zeng, T. Zhou, "A Novel M.M.F Distribution Model for 3-D Analysis of Linear Induction Motor with Asymmetric Cap-Secondary for Metro," *IEEE Trans. Magn.*, vol. 53, no. 9, Art. ID 8107907, 2017.

[4] D. Zeng, G. Lv, T. Zhou, "Equivalent Circuits for Single-Sided Linear Induction Motors with Asymmetric Cap-Secondary for Linear Transit," *IEEE Trans. Energy Convers.*, vol. 33, no.4, pp. 1729–1738, 2018.

[5] J. F. Gieras, "Linear Induction Drives". *Clarendon Press, U.S: New York*, 1994, pp. 1–51.

[6] R. Cao, M. Cheng, B. Zhang, "Speed Control of Complementary and Modular Linear Flux-Switching Permanent-Magnet Motor," *IEEE Trans. Ind. Electron.*, vol. 62, no. 7, pp. 4056-4064, July. 2015.

[7] R. Wai, W. Liu, "Nonlinear control for linear induction motor servo drive," *IEEE Trans. Ind. Electron.*, vol. 50, no. 5, pp. 920–935, Oct. 2003.

[8] R. Wai, C. Chu, "Robust petri fuzzy-neural-network control for linear induction motor drive," *IEEE Trans. Ind. Electron.*, vol. 54, no. 1, pp. 177-189, 2007.

[9] Y. Huang and C. Sung, "Function-based controller for linear motor control systems," *IEEE Trans. Ind. Electron.*, vol. 57, no. 3, pp. 1096–1105, Mar. 2010.

[10] G. Kang, J. H. Kim, and K. Nam, "Parameter estimation scheme for low-speed linear induction motors having different leakage inductances," *IEEE Trans. Ind. Electron.*, vol. 50, no. 4, pp. 708–716, Aug. 2003.

[11] J. Choi, S. Kim, D. S. Yoo, K.H. Kim, "A diagnostic method of simultaneous open-switch faults in inverter-fed linear induction motor drive for reliability enhancement", *IEEE Trans. Ind. Electron.*, vol. 62, no. 15, pp. 4065–4077, Mar. 2015

[12] L. Yan, L. Zhang, Z. Jiao, H. Hu, C. Chen, I. Chen, "Armature reaction field and inductance of coreless moving-coil tubular linear machine," *IEEE Trans. Ind. Electron.*, vol. 61, no.12, pp. 6956–6965, Dec. 2014.

[13] T. Hosobata, A. Yamamoto, T. Higuchi, "Modeling and analysis of a linear resonant electrostatic induction motor considering capacitance imbalance", *IEEE Trans. Ind. Electron.*, vol. 61, no.7, pp. 3439–3447, July. 2014.

[14] R. Cao, M. Cheng, C. Mi, W. Hua, "Influence of leading design parameters on the force performance of a complementary and modular linear flux-switching permanent magnet motor," *IEEE Trans. Ind. Electron.*, vol. 61, no. 5, pp. 2165–2175, May 2014.

[15] Y. Liu, W. Chen, J. Liu, X. Yang, “A high-power linear ultrasonic motor using bending vibration transducer,” *IEEE Trans. Ind. Electron.*, vol. 60, no. 11, pp. 5160–5166, 2013.
[16] S. Yamamura, Theory of Linear Induction Motors. *Tokyo, Japan: Tokyo Univ. Press*, 1978.
[17] R. M. Pai; I. Boldea; S. A. Nasar, “A complete equivalent circuit of a linear induction motor with sheet secondary,” *IEEE Trans. Magn.*, vol. 24, no. 1, pp. 639-654, 1988.
[18] J. Faiz, H. Jafari, “Accurate modeling of single-sided linear induction motor considers end effect and equivalent thickness,” *IEEE Trans. Magn.*, vol. 36, no. 5, pp. 3785–3790, 2000.
[19] S. Nonaka, T. Higuchi, “Approximate Equations for Calculation of Characteristics of Single-Sided Linear Induction Motors,” *Trans. IEEJ.*, vol. 102B, no. 9, pp. 565–572, Sep. 1982.
[20] A. Zare-Bazghaleh, M. Naghashan, A. Khodadoost, “Derivation of Equivalent Circuit Parameters for Single-Sided Linear Induction Motors,” *IEEE Trans. Plasm. Sci.*, vol. 43, no. 10, pp. 3637–3644, 2015.
[21] J. Duncan, “Linear induction motor-equivalent-circuit model,” *IET Elect. Power App.*, vol. 130, no. 1, pp. 51–57, 1983.
[22] E. Amiri; E. A. Mendrela, “A Novel Equivalent Circuit Model of Linear Induction Motors Considering Static and Dynamic End Effects,” *IEEE Trans. Magn.*, vol. 50, no. 3, Art. ID 8200409, 2014.
[23] G. Lv, D. Zeng, T. Zhou, “An Advanced Equivalent Circuit Model for Linear Induction Motors,” *IEEE Trans. Ind. Electron.*, vol. 65, no.9, pp. 7495–7503, 2018.
[24] D. Zeng, G. Lv, T. Zhou and M. Degano, "A Complete Equivalent Circuit Model for Linear Induction Motor Considering Thrust, Vertical and Transversal Forces," 2019 IEEE International Electric Machines & Drives Conference (IEMDC), San Diego, CA, USA, 2019, pp. 1766-1771.
[25] N. Umezu, S. Nakazato, S. Shirasaka, “Characteristics of Double-Sided Linear Induction Motor with Laterally Asymmetric Secondary Conductor”, *Trans. IEEJ.*, vol. 105B, no. 8, pp. 661-668, 1985.

Gang Lv (M’15) received the Ph.D. degree in electric machine and driven from Beijing Jiaotong Univ., China, in 2007.

From 2007 to 2009, he was a Postdoctoral Research Fellow with the Technology Center, CRRC Qingdao Sifang Locomotive and Rolling Stock Co.Ltd., Qingdao, China. In 2007, he joined Sch. of E.E., Beijing Jiaotong Univ., where he is currently a Professor. His research interests include analysis and control of linear machines, ac traction machine, and control.

Dihui Zeng (M’ 16) received the M.Eng. degree in mechatronic engineering from China Univ. of Mining and Technology, China, in 2013, and the Ph.D. degree in electric machine and driven from Beijing Jiaotong Univ., China, in 2019.

From 2013 to 2015, he was a Hardware Engineer with CRRC Zhuzhou Locomotive Institute Co.Ltd., Zhuzhou, China. In 2020, he joined Key Laboratory of Power Electronics and Electric Drive, Institute of E. E., Chinese Academy of Sciences. His research interests include analysis and control of linear machines, Maglev train applications.

Tong Zhou received the B.Eng. degree in electrical engineering from Qingdao Univ., China, in 2013.

He is currently working toward the Ph.D. degree in electric machine and driven in Beijing Jiaotong Univ., China, where he has been engaged in the design and analysis of linear machines, ac traction machine, and control.

Michele Degano (M’15) received his Master’s degree in Electrical Engineering from the University of Trieste, Italy, in 2011, and his Ph.D. degree in Industrial Engineering from the University of Padova, Italy, in 2015. Between 2014 and 2016, he was a post-doctoral researcher at The University of Nottingham, UK, where he joined the Power Electronics, Machines and Control (PEMC) Research Group. In 2016 he was appointed Assistant Professor in Advanced Electrical Machines, at The University of Nottingham, UK. He was promoted Associate Professor in 2020. His main research focuses on electrical machines and drives for industrial, automotive, railway and aerospace applications, ranging from small to large power. He is currently the PEMC Director of Industrial Liaison leading research projects for the development of future hybrid electric aerospace platforms and electric transports.